

Picosecond ion-qubit manipulation and spin-phonon entanglement with resonant laser pulsesW.-X. Guo^{1,2}, Y.-K. Wu^{1,2}, Y.-Y. Huang^{1,2}, L. Feng^{1,2}, C.-X. Huang^{1,2}, H.-X. Yang^{1,3}, J.-Y. Ma^{1,2}, L. Yao³, Z.-C. Zhou^{1,2} and L.-M. Duan^{1,2,*}¹*Center for Quantum Information, Institute for Interdisciplinary Information Sciences, Tsinghua University, Beijing 100084, People's Republic of China*²*Hefei National Laboratory, Hefei 230088, People's Republic of China*³*HYQ Co., Ltd., Beijing 100176, People's Republic of China*

(Received 23 May 2022; accepted 3 August 2022; published 11 August 2022)

Ultrafast spin-phonon entanglement based on spin-dependent momentum kicks (SDKs) provides an approach to realize fast entangling gates with intrinsic robustness and scalability for trapped ion quantum computing. Such SDKs so far have been implemented on a nanosecond timescale by off-resonant Raman transitions where each laser pulse is split into a sequence of perturbation pulses with carefully designed temporal patterns. Here we report an experimental realization of ultrafast qubit manipulation and spin-phonon entanglement in picoseconds using SDKs from single resonant laser pulses on the magnetic-field-insensitive hyperfine qubit states. This experiment demonstrates a convenient approach to ultrafast SDKs on noise-insensitive ion-spin qubits, with improvement in its speed by more than an order of magnitude. It removes the need to engineer the pattern of a sequence of perturbation pulses and is less vulnerable to noise, simplifying the approach to large-scale trapped-ion quantum computing based on fast quantum gates with SDKs.

DOI: [10.1103/PhysRevA.106.022608](https://doi.org/10.1103/PhysRevA.106.022608)**I. INTRODUCTION**

As one of the leading platforms for quantum information processing, ion traps have demonstrated high-fidelity single-qubit and two-qubit gates for up to tens of ions [1–6]. While single-qubit gates are fast and are mainly limited by the available intensity of the control laser or microwave fields [2,7], the two-qubit entangling gates are typically much slower [8] on the order of tens to hundreds of microseconds [2–6]. This is because the commonly used Mølmer-Sørensen gate scheme [9,10] and its variants are restricted to the Lamb-Dicke parameter regime [11], which limits the driving strength that can be applied [8,12]. For larger ion numbers, more complicated pulse sequences are needed to disentangle all the collective phonon modes [13–15], which further increases the gate time. Apart from an undesired overhead for quantum computing, a longer gate time also increases the sensitivity to the environmental noise, constrains the gate performance, and thus causes challenges for fault tolerance [16–18].

To overcome this difficulty, gate schemes based on spin-dependent momentum kicks (SDKs) have been proposed [19–25]. In such schemes, ultrafast laser pulses are applied to the ions to entangle their qubit states with the motional modes beyond the Lamb-Dicke regime; several SDKs arriving in suitable time sequences then disentangle the motional states to obtain qubit-qubit entanglement. Furthermore, when the gate speed is sufficiently faster than the sound speed on the ion array, we further get the advantages that the gate design is independent of the qubit number and can be applied in parallel

for distant ions [26]. At the core of such gate schemes is a high-fidelity SDK for the spin-phonon entanglement operation. Pioneering works have achieved SDKs in nanoseconds [27] for $^{171}\text{Yb}^+$ ions and have further demonstrated two-qubit gates with a fidelity of 76% [28]. In these works, because the level splitting of the hyperfine qubit is smaller than the bandwidth of the laser, an ultrafast laser pulse needs to be split into a sequence of perturbation pulses with carefully designed time intervals to achieve the desired spin dependence. Besides, to realize an entangling gate, the SDKs obtained in this way need to be switched in two opposite directions for efficient accumulation of the displacement. All these requirements increase the experimental complexity and thus reduce the fidelity of the operation.

In this work, we demonstrate spin-phonon entanglement with SDKs on $^{171}\text{Yb}^+$ hyperfine qubits using resonant laser pulses. In our scheme, complicated pulse shaping and splitting are avoided. Compared with the earlier proposal for resonant pulses on optical qubits [29], our scheme uses hyperfine qubits and thus has advantages on qubit coherence time [30]. Previously, ultrafast population transfer from S to P levels has also been achieved in $^{111}\text{Cd}^+$ [31], $^{40}\text{Ca}^+$ [32], and $^{171}\text{Yb}^+$ ions [33], with limited fidelity and without demonstrating the spin-phonon entanglement. Here, by adjusting the intensity of a single laser pulse, we first achieve ultrafast single-qubit π rotation in 2 ps for the hyperfine qubit. Then by applying two pulses from opposite directions, each with half the pulse area, we obtain the desired SDK in 80 ps, which is faster than the previous results by more than an order of magnitude [27]. We further demonstrate the quantum coherence and spin-phonon entanglement under the SDKs by comparing the experimental results with theoretical predictions and by measuring the

*Corresponding author: lmduan@tsinghua.edu.cn

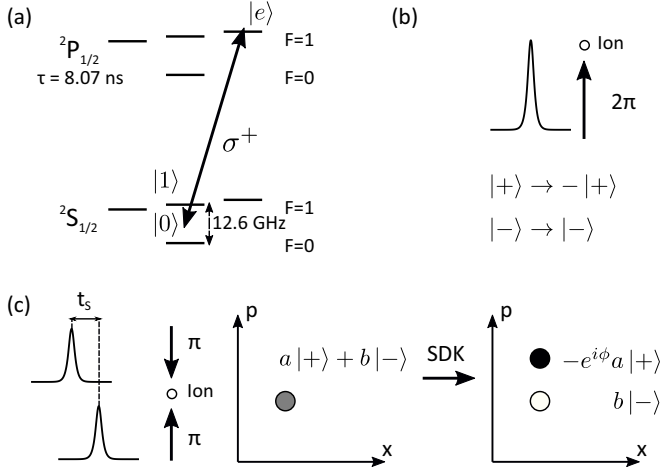


FIG. 1. Experimental scheme. (a) Relevant energy levels of a $^{171}\text{Yb}^+$ ion. The two hyperfine qubit states $|0\rangle$ and $|1\rangle$ are coupled with equal amplitude to an excited state $|e\rangle$ by a resonant ultrafast laser pulse, whose bandwidth is much broader than the qubit frequency ω_{01} . (b) A single laser pulse (indicated by the arrow) drives the Rabi oscillation between the superposition state $|+\rangle \equiv (|0\rangle + |1\rangle)/\sqrt{2}$ and the excited state $|e\rangle$. In particular, when the area of the pulse is set to $\theta = 2\pi$, we get a σ_x gate or a π pulse on the hyperfine qubit. (c) If we apply two ultrafast pulses, each with an area of π , from opposite directions (indicated by the two vertical arrows), we get a spin-dependent momentum kick (SDK). By setting the separation t_s between the two pulses to be a multiple of $2\pi/\omega_{01}$, while $|-\rangle$ is still unchanged, $|+\rangle$ now acquires a minus sign together with a momentum kick from the wave-vector difference between the counterpropagating laser beams. In addition, there is an optical phase, $e^{i\Delta\phi}$, from the path difference of the two beams, which needs to be canceled in the experimental sequence.

Ramsey fringes. Our work largely simplifies the experimental approach to fast entangling gates using SDKs, thus making an important step toward large-scale trapped-ion quantum computing based on fast gates [20,26].

II. SCHEME

Our experimental scheme is sketched in Fig. 1. The qubit states $|0\rangle \equiv |^2S_{1/2}, F=0, m_F=0\rangle$ and $|1\rangle \equiv |^2S_{1/2}, F=1, m_F=0\rangle$ are encoded in the two hyperfine ground states of $^{171}\text{Yb}^+$ ions. These two levels are coupled with equal strength to an excited state, $|e\rangle \equiv |^2P_{1/2}, F=1, m_F=1\rangle$, by a circularly polarized resonant 369-nm laser. The laser has a pulse width of 2 ps and a repetition rate of $2\pi \times 76$ MHz which is locked to a half-integer fraction (1/166.5) of the qubit frequency ω_{01} for reasons that are explained later. The Hamiltonian of the system is given by

$$H = \frac{\omega_{01}}{2} (|1\rangle\langle 1| - |0\rangle\langle 0|) + \omega_m a^\dagger a + \frac{\Omega(t)}{2} |e\rangle \frac{\langle 0| + \langle 1|}{\sqrt{2}} e^{i[\eta(a+a^\dagger)+\phi]} + \text{H.c.}, \quad (1)$$

where a and a^\dagger are the annihilation and the creation operators of the motional state, $\eta \approx 0.083$ is the Lamb-Dicke parameter, and ϕ is the optical phase of the laser. Since the pulse duration of $\Delta t = 2$ ps is much shorter than the timescale for the

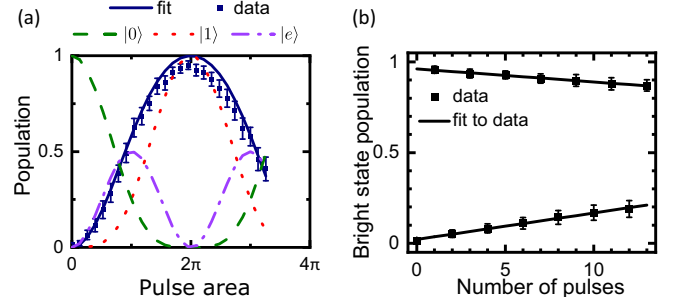


FIG. 2. Ultrafast single-qubit operation in 2 ps. By adjusting the intensity I of a single laser pulse, we get Rabi oscillation between $|+\rangle$ and $|e\rangle$ versus the pulse area $\theta \propto \sqrt{I}$. When $\theta = 2\pi$, we get $U = -|+\rangle\langle +| + |-\rangle\langle -| = -\sigma_x$ as a single-qubit π pulse. (a) By initializing the qubit in $|0\rangle$ (a dark state under the detection laser), we scan the bright-state population versus the pulse area as the blue dots. Each data point is averaged over 100 samples with error bars representing one standard deviation. The green dashed line, the red dotted line, and the purple dash-dotted line are the theoretical evolutions for populations in $|0\rangle$, $|1\rangle$, and $|e\rangle$, respectively. Together, we compute the theoretical evolution of the bright state population as the blue solid curve, which agrees well with the experimental result. (b) By tuning the laser intensity to the fitted peak in panel (a), we obtain the desired ultrafast single-qubit π pulse. Starting from $|0\rangle$, we further measure the population in the bright state versus the pulse number: ideally, after an even number of pulses the qubit shall remain in the dark state, while an odd number of pulses flip the qubit into the bright state. Experimentally, we fit the slope of the two sets of data as $(1.46 \pm 0.05)\%$ and $-(0.72 \pm 0.03)\%$, which gives an average gate error of 1.1%. The asymmetry between these two errors can come from the leakage to the other S or P levels due to, e.g., the imperfect laser polarization or pulse length, which are more likely to result in a bright state.

qubit frequency $\omega_{01} = 2\pi \times 12.6$ GHz or the trap frequency $\omega_m = 2\pi \times 1.25$ MHz ($\omega_{01}\Delta t \ll 1$ and $\omega_m\Delta t \ll 1$), $\Omega(t)$ can be regarded as a delta function $\Omega(t) = \theta\delta(t - t_0)$, where θ is the pulse area and t_0 is the arriving time. Then the unitary evolution of the system can be divided into two parts: around a laser pulse, we have

$$U_p = |-\rangle\langle -| + (|+\rangle\langle +| + |e\rangle\langle e|) \cos \frac{\theta}{2} - i\{|e\rangle\langle +| e^{i[\eta(a+a^\dagger)+\phi]} + \text{H.c.}\} \sin \frac{\theta}{2}, \quad (2)$$

which is a transition between $|+\rangle \equiv (|0\rangle + |1\rangle)/\sqrt{2}$ and $|e\rangle$ accompanied by a momentum kick, with the state $|-\rangle \equiv (|0\rangle - |1\rangle)/\sqrt{2}$ left unchanged; in the rest of the time, the system evolves freely with the spin state oscillating between $|\pm\rangle$ at the frequency ω_{01} and the motional state rotating at ω_m . More details about the experimental setup can be found in Appendix A.

III. ULTRAFAST SINGLE-QUBIT π PULSE

First we calibrate the effect of a single pulse. When the qubit is initialized in $|0\rangle$, we can plot the theoretical population in $|0\rangle$, $|1\rangle$, and $|e\rangle$ versus the pulse area θ as shown in Fig. 2(a). Experimentally, we can measure the bright state

population after the laser pulse, which contains the population in $|1\rangle$ together with $2/3$ of the population in $|e\rangle$ (during the detection cycle, $|e\rangle$ has $1/3$ probability to decay to the dark state $|0\rangle$, and $2/3$ probability to decay to the Zeeman levels of the $^2S_{1/2}$, $F = 1$ manifold which are bright states [34]), versus the square root of the laser intensity. Fitted by the blue solid curve, we can thus calibrate the pulse area θ for different laser intensities. In particular, in Fig. 2(b) we set $\theta = 2\pi$ for an ultrafast single-qubit π pulse. By repeatedly applying this π pulse, we observe alternating oscillation between $|0\rangle$ and $|1\rangle$ for even and odd numbers of pulses, and we fit an average gate error of 1.1%. This gate of 2 ps is faster than that of the previous work on the hyperfine qubit using off-resonant Raman transitions [35] and is comparable to those coherent excitations to P levels achieved using resonant pulses which have lower fidelities [31–33].

IV. ULTRAFAST SDK

An SDK can be constructed using two laser pulses with $\theta = \pi$ from opposite directions with an interval of t_s , as shown in Fig. 1(c). The first pulse transfers $|+\rangle$ to $|e\rangle$ with a momentum kick while leaving $|-\rangle$ unchanged, and then the second pulse brings $|e\rangle$ back to $|+\rangle$ with a further momentum kick and still keeps $|-\rangle$ untouched. Together, the two pulses constitute an SDK in the form of $U_{\text{SDK}} = |-\rangle\langle -| - |+\rangle\langle +|e^{i[2\eta(a+a^\dagger)+\Delta\phi]}$ where we restrict ourselves to the qubit subspace (below we say this SDK is active on $|+\rangle$ since the momentum kick is only applied to the $|+\rangle$ state). To achieve high fidelity, we want $\Gamma t_s \ll 1$ where $\Gamma = 2\pi \times 20$ MHz is the natural linewidth of the excited state $|e\rangle$. Also note that the qubit states are oscillating between $|\pm\rangle$ during the free evolution, so we set $t_s = 2\pi/\omega_{01} = 79.4$ ps such that the two counterpropagating pulses are in phase on the ion. Note that this SDK is faster than those in previous works by an order of magnitude [27,28], which gives us stronger insensitivity to the secular motion or micromotion. Although this choice of t_s gives us a spontaneous emission error of about $\Gamma t_s \approx 1\%$ for this experiment, we should mention that this is not a fundamental limit for this scheme: if faster pulses on the order of 100 fs are used, we can set t_s to be on the same order to avoid overlap between the two pulses, but this time the spontaneous emission will be much smaller and the error will be limited by the qubit state rotation during t_s as $(\omega_{01}t_s)^2 \sim 10^{-4}$; besides, this will give us even faster SDKs.

The above SDK contains a phase difference of $\Delta\phi$ between the optical paths of the two counterpropagating laser pulses. While this phase is stable in a single experimental trial, there can be slow drifts on the timescale of seconds and thus this can influence the experimental result when we average over a large number of trials. Therefore, this optical phase needs to be canceled in the design of the entangling gate. A simple scheme is to have equal numbers of SDKs that are active on the two spin-dependent phase-space trajectories. In this way, the optical phase becomes an irrelevant global phase.

We demonstrate this idea in Fig. 3 by applying two SDKs (each consists of two ultrafast pulses separated by t_s) with a time interval τ on a qubit initialized in $|0\rangle$. First let us ignore the optical phase for a moment. If we select $\tau = 2\pi k/\omega_{01}$ between the two SDKs where k is an integer, the $|\pm\rangle$ states

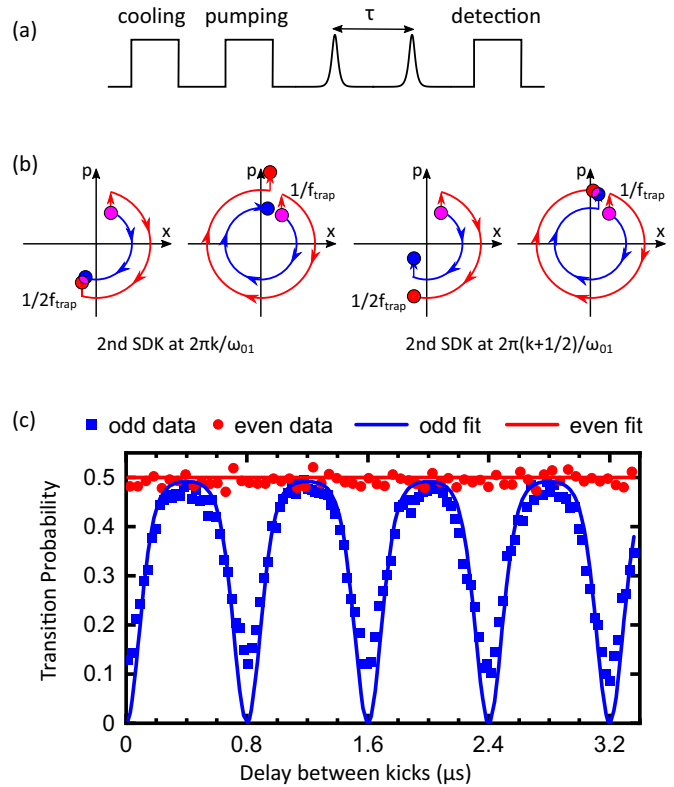


FIG. 3. Ultrafast spin-phonon entanglement by SDK. (a) The qubit and the phonon states are initialized by Doppler cooling followed by optical pumping [11]. Then we apply two SDKs with a separation of τ and finally we measure the qubit state. (b) Schematic evolution in the phase space of the phonon mode. The qubit is initialized in $|0\rangle$ (purple or light gray circles), which is a superposition of $|+\rangle$ (red, outer trajectories) and $|-\rangle$ (blue, inner trajectories). An SDK leads to a displacement for $|+\rangle$ while keeping $|-\rangle$ unchanged and thus creates spin-phonon entanglement. Then the phonon state rotates at the angular frequency ω_m (arcs in the clockwise direction) and in the meantime the spin states $|+\rangle$ and $|-\rangle$ evolve into each other at the qubit frequency ω_{01} (not shown). The two left subplots: If we apply the second SDK at $\tau = 2\pi k/\omega_{01}$, the two momentum kicks will act on the same trajectory. When τ is around half a trap period, the two trajectories meet again and hence the spin and the phonon states disentangle; while if τ is around a full trap period, the two trajectories are further separated to give stronger entanglement. The two right subplots: If we apply the second SDK at $\tau = 2\pi(k + 1/2)/\omega_{01}$, the two momentum kicks will act on the two trajectories separately. This time, we get the largest spin-phonon entanglement when τ is around half a trap period, and zero for a full trap period. (c) Measured evolution of the bright state population. When $\tau = 2\pi(k + 1/2)/\omega_{01}$ (blue squares), we get oscillation vs τ as the spin and photon states entangle and disentangle. On the other hand, if we choose $\tau = 2\pi k/\omega_{01}$ (red dots), the uncontrolled optical phase accumulates, and thus the average value over 100 samples stays around 0.5 independent of the separation time τ .

evolve back to themselves during the interval such that both SDKs are active on the same path in the phase space as shown in the left panels of Fig. 3(b). In such cases, when τ is close to half a period of the phonon mode, the two spin-dependent trajectories recombine after the two SDKs so that the spin and the

phonon states disentangle; on the other hand, when τ is close to a full motional period, the two trajectories are further split apart to give larger spin-phonon entanglement. If, instead, we set $\tau = 2\pi(k + 1/2)/\omega_{01}$ between the two SDKs, the original $|+\rangle$ ($|-\rangle$) state at the first SDK will evolve into $|-\rangle$ ($|+\rangle$) at the second SDK, so that the two SDKs will be active on the two trajectories individually. Then the above statements are reversed [right panels of Fig. 3(b)]: when τ is close to half a trap period, we get large spin-phonon entanglement, and when τ is around a full trap period, the spin and the phonon state disentangle.

From the above arguments, one would expect there to be oscillatory behavior in the measured population in $|1\rangle$: without spin-phonon entanglement, we expect the qubit state to be close to the initial one and thus there would be low population in $|1\rangle$; at large spin-phonon entanglement, since the displacement of 4η in the phase space is large compared with the wave packet of the ion at the Doppler temperature (see Appendix B), we get roughly an equal mixture of $|+\rangle$ and $|-\rangle$ and thus a population of about 50% in $|1\rangle$. Now we include the effect of the uncontrolled optical phase. When $\tau = 2\pi k/\omega_{01}$, since the two SDKs are active for the same trajectory, the optical phases accumulate and thus the spin states average to $(|+\rangle\langle +| + |-\rangle\langle -|)/2$ independent of τ , as shown by the red curve in Fig. 3(c). When $\tau = 2\pi(k + 1/2)/\omega_{01}$, the two optical phases cancel, and therefore, we get the expected oscillation as shown by the blue curve.

To further demonstrate the quantum coherence in this scheme, we perform a Ramsey experiment: We initialize the qubit state in $|+\rangle$ by a microwave field $\pi/2$ pulse with detuning $\delta\omega$ to the qubit frequency ω_{01} , wait for time $T = 50 \mu\text{s}$, and then apply a second microwave $\pi/2$ pulse and measure the qubit state. During the idling time, we insert two SDKs separated by $\tau = 2\pi(k + 1/2)/\omega_{01}$ with $k = 10$ 156 such that $\tau = 0.803 \mu\text{s}$ is close to a full period of the phonon mode. Ideally, this amounts to a global optical phase and a global momentum kick independent of the spin state; thus, we expect high Ramsey fringe contrast close to 1. In the experiment we measure a contrast of about 0.78 as shown in Fig. 4, or about 11% deviation in the measured population. This can be explained by 4.4% error from the four pulses (slope of Fig. 2), 4% spontaneous emission, and 3% state preparation and measurement error (intercept of Fig. 2).

V. DISCUSSION

Our scheme of generating SDKs using resonant pulses does not require splitting each pulse into multiple segments with carefully controlled temporal patterns. Besides, the SDKs we obtain are in the form of $U_{\text{SDK}} = |-\rangle\langle -| - |+\rangle\langle +| e^{i[2\eta(a+a^\dagger) + \Delta\phi]}$. By suitably locking the repetition rate of the pulsed laser as shown above, such SDKs can directly accumulate so that high gate speed can be achieved without the need to switch pulse directions [28,36]. Therefore, it shall be more convenient for experiments and less vulnerable to noise. To cancel the uncontrolled optical phase which may have long-term drift, we require an equal number of SDKs that are active on $|+\rangle$ and $|-\rangle$. Although this seems to put some restriction on the available gate schemes, we would

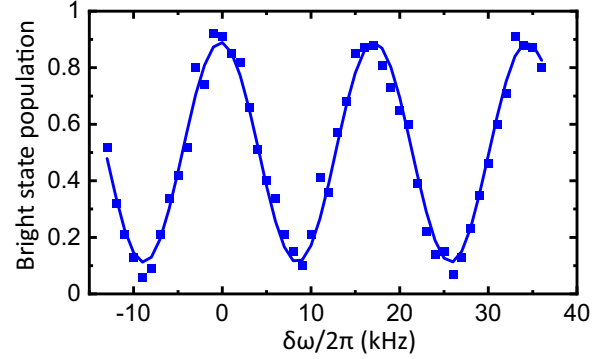


FIG. 4. We initialize the qubit in $|+\rangle$ by a $\pi/2$ microwave pulse, wait for time T where we insert two SDKs separated by $t_s = 2\pi(k + 1/2)/\omega_{01}$, and then apply another $\pi/2$ microwave pulse and measure the final qubit state. For a fixed $T = 50 \mu\text{s}$ and $\tau = 0.803 \mu\text{s}$, we scan the detuning $\delta\omega$ between the frequency of the microwave and the qubit. A contrast of 0.78 is extracted from the Ramsey fringes.

like to mention that it still covers many of the previous gate schemes based on SDKs. As a special example, if we always apply paired SDKs on $|+\rangle$ and $|-\rangle$ with $\tau \approx \pi/\omega_m$, we get a combined SDK in the form of $U = e^{2i\eta(a+a^\dagger)\sigma_x}$. This unitary operation, up to an exchange of σ_z and σ_x bases, is equivalent to the SDKs considered in Refs. [27,28] and thus can be used to further construct various ultrafast two-qubit entangling gates [19–25]. Besides, now we have the additional degrees of freedom for asymmetric paths for $|\pm\rangle$; hence, more general gate schemes may be achieved.

Also note that, in this work we only implement an ultrafast single-qubit σ_x operation, which is not universal for quantum computing [17]. On the one hand, such a universal gate set for single-qubit rotations using a pulsed laser may not be necessary because it is not difficult to achieve high-fidelity single-qubit gates on a microsecond timescale and below using continuous-wave lasers or microwaves [2,3,7]. On the other hand, for certain tasks such as preparing the initial state $|+\rangle$ from $|0\rangle$ in this experiment, we could also use the ultrafast pulsed laser together with the free evolution: Specifically, a first pulse with area $\theta = \pi$ can transform $|0\rangle$ into $(|-\rangle + |e\rangle)/\sqrt{2}$; a free evolution time of π/ω_{01} then rotates $|-\rangle$ into $|+\rangle$; and finally a second pulse with area $\theta = \pi/2$ can bring $(|+\rangle + |e\rangle)/\sqrt{2}$ into $|+\rangle$. Note that these two pulses should come from the same direction to avoid any entanglement to the phonon state.

ACKNOWLEDGMENTS

We thank Y. Wang for experimental assistance in trap assembling and M.-L. Cai for helpful discussions. This work is supported by the Innovation Program for Quantum Science and Technology (Grant No. 2021ZD0301601), the Tsinghua University Initiative Scientific Research Program, and the Frontier Science Center for Quantum Information of the Ministry of Education of China. Y.-K.W. acknowledges support from the start-up fund from Tsinghua University.

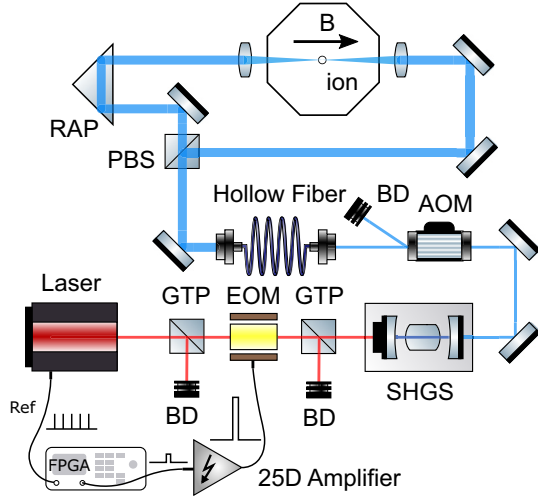


FIG. 5. Experimental setup. The mode-locked 739-nm pulsed laser first goes through our pulse selection system which consists of two Glan-Taylor polarizers (GTP) and an electro-optic modulator (EOM). The EOM is driven by an amplifier which can convert the TTL signal to a 175-V Vpp pulse signal. A second harmonic generator system (SHGS) then converts the laser wavelength to 369.5 nm. An acousto-optic modulator (AOM) is used to further suppress the stray light, whose zeroth-order light is blocked by a beam dump (BD) while the first-order light is coupled to a hollow fiber and is split into two beams by a polarization beam splitter (PBS). A right-angle prism (RAP) serves as a delay stage to adjust the relative distance of the two beams. The quantization axis of the ion is set along the laser beams by a magnetic field so that we can get a pure circular polarization.

APPENDIX A: EXPERIMENTAL SETUP

The detailed experimental setup is shown in Fig. 5. We use Coherent Mira 900 to generate the pulsed laser, with a 2-ps pulse width, a 76-MHz repetition rate, and a typical power of 2.4 W. The wavelength is tuned to 739 nm so that it can be resonant with the $S_{1/2} \rightarrow P_{1/2}$ transition frequency after the second harmonic generator system (SHGS). The pulse picking system consists of a Conoptics M350-160 electro-optic modulator (EOM), whose half-wave voltage is about 192 V, and two Glan-Taylor polarizers. A field-programmable gate array (FPGA) locked to the repetition rate is used to trigger a Conoptics 25D amplifier so that the amplifier can output a 175-V signal in 8 ns to drive the EOM and to select the desired pulse to go through the polarizer.

Although we only achieve a 50:1 extinction ratio by the EOM, the SHGS can raise the extinction ratio to about 40 000:1 owing to its nonlinear effect (see Fig. 6). Given that each experimental trial may take milliseconds, such a weak stray light may still not be negligible, so we further add an acousto-optic modulator (AOM) to restrict the pass window of the pulsed laser to 3 μ s.

After a hollow fiber, the pulsed laser is split into two counterpropagating beams which are finally focused on the ion by homemade objectives. Given an estimated focal spot size of about $10 \mu\text{m}^2$, theoretically we need a pulse energy of 26.2 pJ (or 2-mW average laser power) to reach a π -pulse area. In our experiment, we have more than 200-mW laser power after the SHGS, but only about 20 mW is actu-

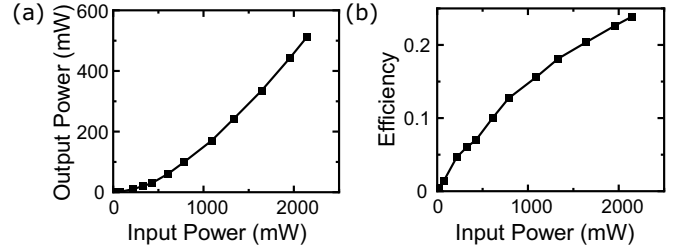


FIG. 6. Experimental calibration of the SHGS under different input power of the 739-nm laser. (a) The output 370-nm laser power vs the input laser power. (b) The frequency doubling efficiency. With the EOM switched on (off), we get about 1.5-W (about 30 mW) laser power from the pulse selection system in Fig. 5, which in turn becomes more than 200 mW (about 5 μ W) after the SHGS due to the nonlinear frequency doubling effect. This gives us an extinction ratio above 40 000:1.

ally applied on the ion due to the insufficient voltage from the amplifier, the AOM diffraction efficiency, and the fiber loss.

APPENDIX B: THEORETICAL EVOLUTION UNDER THERMAL MOTION

Here we consider the theoretical evolution for the blue curve in Fig. 3(c) of the main text. Since we apply two SDKs on the two paths, the shared optical phase can be removed. Working in the interaction picture of $H_0 = \frac{\omega_{01}}{2}(|1\rangle\langle 1| - |0\rangle\langle 0|) + \omega_m a^\dagger a$, the two SDKs can be expressed as

$$U_1 = |-\rangle\langle -| - |+\rangle\langle +| + |e^{2i\eta(\alpha + \alpha^\dagger)}\rangle\rangle = |-\rangle\langle -| - |+\rangle\langle +| + |D(2i\eta)\rangle\rangle \quad (\text{B1})$$

and

$$U_2 = |+\rangle\langle +| - |-\rangle\langle -| - |e^{2i\eta(\alpha e^{-i\omega_m\tau} + \alpha^\dagger e^{i\omega_m\tau})}\rangle\rangle = |+\rangle\langle +| - |-\rangle\langle -| - |D(2i\eta e^{i\omega_m\tau})\rangle\rangle, \quad (\text{B2})$$

where we use the fact that $\omega_{01}\tau = 2\pi(k + 1/2)$. An initial state $|0\rangle \otimes |\alpha\rangle$ will become $U_1|0\rangle \otimes |\alpha\rangle = [|-\rangle|\alpha\rangle - e^{i\eta(\alpha + \alpha^*)}|+\rangle|\alpha + 2i\eta\rangle] / \sqrt{2}$ after the first SDK, and $U_2 U_1 |0\rangle \otimes |\alpha\rangle = -[e^{i\eta(\alpha + \alpha^*)}|+\rangle|\alpha + 2i\eta\rangle + e^{i\eta(\alpha e^{-i\omega_m\tau} + \alpha^* e^{i\omega_m\tau})}|-\rangle|\alpha + 2i\eta e^{i\omega_m\tau}\rangle] / \sqrt{2}$. Moving back to the laboratory frame, we have the final state

$$\frac{1}{\sqrt{2}} [e^{i\eta(\alpha + \alpha^*)}|-\rangle|\alpha + 2i\eta\rangle e^{-i\omega_m\tau} + e^{i\eta(\alpha e^{-i\omega_m\tau} + \alpha^* e^{i\omega_m\tau})}|+\rangle|\alpha e^{-i\omega_m\tau} + 2i\eta\rangle], \quad (\text{B3})$$

where we discard a global phase. This expression corresponds to the right panels of Fig. 3(b) in the main text.

Now we consider an initial thermal motional state, ρ_m , with an average phonon number, \bar{n} . Together, the two SDKs map the initial state $|0\rangle\langle 0| \otimes \rho_m$ into

$$\begin{aligned} \rho(\tau) &= U_2 U_1 |0\rangle\langle 0| \otimes \rho_m U_1^\dagger U_2^\dagger \\ &= \frac{1}{2} |+\rangle\langle +| \otimes D(2i\eta) \rho_m D(-2i\eta) \\ &\quad + \frac{1}{2} |-\rangle\langle -| \otimes D(2i\eta e^{i\omega_m\tau}) \rho_m D(-2i\eta e^{i\omega_m\tau}) \end{aligned}$$

$$\begin{aligned}
& + \frac{1}{2} |+\rangle\langle -| \otimes D(2i\eta)\rho_m D(-2i\eta e^{i\omega_m\tau}) \\
& + \frac{1}{2} |-\rangle\langle +| \otimes D(2i\eta e^{i\omega_m\tau})\rho_m D(-2i\eta). \quad (\text{B4})
\end{aligned}$$

Finally we trace out the phonon state to get the reduced density matrix of the spin state:

$$\begin{aligned}
\rho_s(\tau) & = \text{Tr}_m[\rho(\tau)] \\
& = \frac{1}{2} [|+\rangle\langle +| + |-\rangle\langle -| \\
& \quad + (|+\rangle\langle -| e^{-i\theta} + |-\rangle\langle +| e^{i\theta}) \\
& \quad \times e^{-8\eta^2(\bar{n} + \frac{1}{2})(1 - \cos \omega_m\tau)}], \quad (\text{B5})
\end{aligned}$$

where $\theta = 4\eta^2 \sin \omega_m\tau$. The population in the bright state $|1\rangle$ is thus

$$P_1(\tau) = \frac{1}{2} [1 - \cos(4\eta^2 \sin \omega_m\tau) e^{-8\eta^2(\bar{n} + \frac{1}{2})(1 - \cos \omega_m\tau)}]. \quad (\text{B6})$$

From this expression, we can see that when $\omega_m\tau = 2k\pi$, namely, a multiple of a full trap period, P_1 returns to its initial value of zero. On the other hand, when $\omega_m\tau = (2k + 1)\pi$, namely, an odd multiple of half a trap period, the population is highest, and when $16\eta^2(\bar{n} + 1/2) \gg 1$, it saturates around 50%. We use this expression to fit the experimental data in Fig. 3(c) of the main text and get an average phonon number of $\bar{n} \approx 37$.

-
- [1] T. P. Harty, D. T. C. Allcock, C. J. Ballance, L. Guidoni, H. A. Janacek, N. M. Linke, D. N. Stacey, and D. M. Lucas, High-Fidelity Preparation, Gates, Memory, and Readout of a Trapped-Ion Quantum Bit, *Phys. Rev. Lett.* **113**, 220501 (2014).
- [2] C. J. Ballance, T. P. Harty, N. M. Linke, M. A. Sepiol, and D. M. Lucas, High-Fidelity Quantum Logic Gates Using Trapped-Ion Hyperfine Qubits, *Phys. Rev. Lett.* **117**, 060504 (2016).
- [3] J. P. Gaebler, T. R. Tan, Y. Lin, Y. Wan, R. Bowler, A. C. Keith, S. Glancy, K. Coakley, E. Knill, D. Leibfried, and D. J. Wineland, High-Fidelity Universal Gate Set for $^9\text{Be}^+$ Ion Qubits, *Phys. Rev. Lett.* **117**, 060505 (2016).
- [4] Ye Wang, S. Crain, C. Fang, B. Zhang, S. Huang, Q. Liang, P. H. Leung, K. R. Brown, and J. Kim, High-Fidelity Two-Qubit Gates Using a Microelectromechanical-System-Based Beam Steering System for Individual Qubit Addressing, *Phys. Rev. Lett.* **125**, 150505 (2020).
- [5] I. Pogorelov, T. Feldker, Ch. D. Marciniak, L. Postler, G. Jacob, O. Kriegelsteiner, V. Podlesnic, M. Meth, V. Negnevitsky, M. Stadler, B. Höfer, C. Wächter, K. Lakhmanskiy, R. Blatt, P. Schindler, and T. Monz, Compact ion-trap quantum computing demonstrator, *PRX Quantum* **2**, 020343 (2021).
- [6] L. Egan, D. M. Debroy, C. Noel, A. Risinger, D. Zhu, D. Biswas, M. Newman, M. Li, K. R. Brown, M. Cetina *et al.*, Fault-tolerant control of an error-corrected qubit, *Nature (London)* **598**, 281 (2021).
- [7] D. P. L. Aude Craik, N. M. Linke, T. P. Harty, C. J. Ballance, D. M. Lucas, A. M. Steane, and D. T. C. Allcock, Microwave control electrodes for scalable, parallel, single-qubit operations in a surface-electrode ion trap, *Appl. Phys. B* **114**, 3 (2014).
- [8] A. Steane, C. F. Roos, D. Stevens, A. Mundt, D. Leibfried, F. Schmidt-Kaler, and R. Blatt, Speed of ion-trap quantum-information processors, *Phys. Rev. A* **62**, 042305 (2000).
- [9] G. J. Milburn, S. Schneider, and D. F. V. James, Ion trap quantum computing with warm ions, *Fortschr. Phys.* **48**, 801 (2000).
- [10] A. Sørensen and K. Mølmer, Entanglement and quantum computation with ions in thermal motion, *Phys. Rev. A* **62**, 022311 (2000).
- [11] D. Leibfried, R. Blatt, C. Monroe, and D. Wineland, Quantum dynamics of single trapped ions, *Rev. Mod. Phys.* **75**, 281 (2003).
- [12] V. M. Schäfer, C. J. Ballance, K. Thirumalai, L. J. Stephenson, T. G. Ballance, A. M. Steane, and D. M. Lucas, Fast quantum logic gates with trapped-ion qubits, *Nature (London)* **555**, 75 (2018).
- [13] Shi-Liang Zhu, C. Monroe, and L.-M. Duan, Arbitrary-speed quantum gates within large ion crystals through minimum control of laser beams, *Europhys. Lett.* **73**, 485 (2006).
- [14] T. J. Green and M. J. Biercuk, Phase-Modulated Decoupling and Error Suppression in Qubit-Oscillator Systems, *Phys. Rev. Lett.* **114**, 120502 (2015).
- [15] P. H. Leung, K. A. Landsman, C. Figgatt, N. M. Linke, C. Monroe, and K. R. Brown, Robust 2-Qubit Gates in a Linear Ion Crystal Using a Frequency-Modulated Driving Force, *Phys. Rev. Lett.* **120**, 020501 (2018).
- [16] D. Gottesman, Theory of fault-tolerant quantum computation, *Phys. Rev. A* **57**, 127 (1998).
- [17] M. A. Nielsen and I. L. Chuang, *Quantum Computation and Quantum Information*, 10th ed. (Cambridge University, Cambridge, England, 2010).
- [18] E. T. Campbell, B. M. Terhal, and C. Vuillot, Roads towards fault-tolerant universal quantum computation, *Nature (London)* **549**, 172 (2017).
- [19] J. J. García-Ripoll, P. Zoller, and J. I. Cirac, Speed Optimized Two-Qubit Gates with Laser Coherent Control Techniques for Ion Trap Quantum Computing, *Phys. Rev. Lett.* **91**, 157901 (2003).
- [20] L.-M. Duan, Scaling Ion Trap Quantum Computation through Fast Quantum Gates, *Phys. Rev. Lett.* **93**, 100502 (2004).
- [21] J. Mizrahi, B. Neyenhuis, K. G. Johnson, W. C. Campbell, C. Senko, D. Hayes, and C. Monroe, Quantum control of qubits and atomic motion using ultrafast laser pulses, *Appl. Phys. B* **114**, 45 (2014).
- [22] C. D. B. Bentley, A. R. R. Carvalho, and J. J. Hope, Trapped ion scaling with pulsed fast gates, *New J. Phys.* **17**, 103025 (2015).
- [23] M. I. Hussain, M. J. Petrasianas, C. D. B. Bentley, R. L. Taylor, A. R. R. Carvalho, J. J. Hope, E. W. Streed, M. Lobino, and D. Kielpinski, Ultrafast, high repetition rate, ultraviolet, fiber-laser-based source: Application towards Yb^+ fast quantum-logic, *Opt. Express* **24**, 16638 (2016).
- [24] A. K. Ratcliffe, R. L. Taylor, J. J. Hope, and A. R. R. Carvalho, Scaling Trapped Ion Quantum Computers Using Fast Gates and Microtraps, *Phys. Rev. Lett.* **120**, 220501 (2018).
- [25] E. P. G. Gale, Z. Mehdi, L. M. Oberg, A. K. Ratcliffe, S. A. Haine, and J. J. Hope, Optimized fast gates for quantum computing with trapped ions, *Phys. Rev. A* **101**, 052328 (2020).

- [26] Y.-K. Wu and L.-M. Duan, A two-dimensional architecture for fast large-scale trapped-ion quantum computing, *Chin. Phys. Lett.* **37**, 070302 (2020).
- [27] J. Mizrahi, C. Senko, B. Neyenhuis, K. G. Johnson, W. C. Campbell, C. W. S. Conover, and C. Monroe, Ultrafast Spin-Motion Entanglement and Interferometry with a Single Atom, *Phys. Rev. Lett.* **110**, 203001 (2013).
- [28] J. D. Wong-Campos, S. A. Moses, K. G. Johnson, and C. Monroe, Demonstration of Two-Atom Entanglement with Ultrafast Optical Pulses, *Phys. Rev. Lett.* **119**, 230501 (2017).
- [29] E. Torrontegui, D. Heinrich, M. I. Hussain, R. Blatt, and J. J. García-Ripoll, Ultra-fast two-qubit ion gate using sequences of resonant pulses, *New J. Phys.* **22**, 103024 (2020).
- [30] P. Wang, C.-Y. Luan, M. Qiao, M. Um, J. Zhang, Y. Wang, X. Yuan, M. Gu, J. Zhang, and K. Kim, Single ion qubit with estimated coherence time exceeding one hour, *Nat. Commun.* **12**, 233 (2021).
- [31] M. J. Madsen, D. L. Moehring, P. Maunz, R. N. Kohn, L.-M. Duan, and C. Monroe, Ultrafast Coherent Excitation of a Trapped Ion Qubit for Fast Gates and Photon Frequency Qubits, *Phys. Rev. Lett.* **97**, 040505 (2006).
- [32] D. Heinrich, M. Guggemos, M. Guevara-Bertsch, M. I. Hussain, C. F. Roos, and R. Blatt, Ultrafast coherent excitation of a $^{40}\text{Ca}^+$ ion, *New J. Phys.* **21**, 073017 (2019).
- [33] K. Shimizu, J. Scarabel, E. Bridge, S. Connell, M. Ghadimi, B. Haylock, M. I. Hussain, E. Streed, and M. Lobino, Ultrafast coherent excitation of an ytterbium ion with single laser pulses, *Appl. Phys. Lett.* **119**, 214003 (2021).
- [34] S. Olmschenk, K. C. Younge, D. L. Moehring, D. N. Matsukevich, P. Maunz, and C. Monroe, Manipulation and detection of a trapped Yb^+ hyperfine qubit, *Phys. Rev. A* **76**, 052314 (2007).
- [35] W. C. Campbell, J. Mizrahi, Q. Quraishi, C. Senko, D. Hayes, D. Hucul, D. N. Matsukevich, P. Maunz, and C. Monroe, Ultrafast Gates for Single Atomic Qubits, *Phys. Rev. Lett.* **105**, 090502 (2010).
- [36] K. G. Johnson, J. D. Wong-Campos, B. Neyenhuis, J. Mizrahi, and C. Monroe, Ultrafast creation of large Schrödinger cat states of an atom, *Nat. Commun.* **8**, 697 (2017).